

The dark matter halos of massive, relaxed galaxy clusters observed with Chandra

R. W. Schmidt¹* and S. W. Allen²

¹ *Astronomisches Rechen-Institut, Zentrum für Astronomie der Universität Heidelberg, Mönchhofstrasse 12-14, 69120 Heidelberg, Germany*
² *Kavli Institute for Particle Astrophysics and Cosmology, Stanford University, 382 Via Pueblo Mall, Stanford, CA 94305-4060, USA*

Draft December 2, 2024

ABSTRACT

We use the Chandra X-ray Observatory to study the dark matter halos of 34 massive, dynamically relaxed galaxy clusters, spanning the redshift range $0.06 < z < 0.7$. The observed dark matter and total mass (dark-plus-luminous matter) profiles can be approximated by the Navarro Frenk & White (hereafter NFW) model for cold dark matter (CDM) halos; for ~ 80 per cent of the clusters, the NFW model provides a statistically acceptable fit. In contrast, the singular isothermal sphere model can, in almost every case, be completely ruled out. We observe a well-defined mass-concentration relation for the clusters with a normalization and intrinsic scatter in good agreement with the predictions from simulations. The slope of the mass-concentration relation, $c \propto M_{\text{vir}}^a / (1+z)^b$ with $a = -0.41 \pm 0.11$ at 95 per cent confidence, is steeper than the value $a \sim -0.1$ predicted by CDM simulations for lower mass halos. With the slope a included as a free fit parameter, the redshift evolution of the concentration parameter, $b = 0.54 \pm 0.47$ at 95 per cent confidence, is also slower than, but marginally consistent with, the same simulations ($b \sim 1$). Fixing $a \sim -0.1$ leads to an apparent evolution that is significantly slower, $b = 0.20 \pm 0.45$, although the goodness of fit in this case is significantly worse. Using a generalized NFW model, we find the inner dark matter density slope, α , to be consistent with unity at 95 per cent confidence for the majority of clusters. Combining the results for all clusters for which the generalized NFW model provides a good description of the data, we measure $\alpha = 0.88 \pm 0.29$ at 95 per cent confidence, in agreement with CDM model predictions.

Key words: cosmology: observations – dark matter – X-rays: galaxies: clusters

1 INTRODUCTION

One of the most remarkable results of cold dark matter (CDM) simulations of structure formation is that the density profiles of dark matter halos on all resolvable mass scales, from small satellites to the most massive galaxy clusters, can be approximated by a universal profile, the so-called Navarro-Frenk-White (NFW) profile (Navarro, Frenk & White 1995, 1997)

$$\rho(r) = \frac{\rho_0}{(\frac{r}{r_s})(1 + \frac{r}{r_s})^2}. \quad (1)$$

Here r_s is the characteristic scale radius of the halo and ρ_0 is the central density. The model has a central, negative logarithmic density slope, referred to hereafter as the “inner slope”

$$\alpha = -\frac{d \log \rho}{d \log r} \Big|_{r \rightarrow 0} = 1. \quad (2)$$

* E-mail: rschmidt@ari.uni-heidelberg.de

NFW also defined the concentration parameter, c , as the ratio of r_{200} , the radius within which the matter density is 200 times the critical density, and the scale radius:

$$c = \frac{r_{200}}{r_s}. \quad (3)$$

They showed that smaller mass halos are more concentrated than the higher mass halos and interpreted this as reflecting the higher formation redshift of the lower mass systems.

Copious numerical work has been devoted to testing these fundamental findings. To explain the mass-concentration relation and its redshift evolution, Bullock et al. (2001) introduced a simple, but highly successful model for the formation of dark matter halos. In this model, only two parameters, K , which determines the initial concentration parameter of collapsing halos and F , the ratio of the initial collapse mass to the final virial mass of the halo at redshift zero, are required to approximately match the simulation predictions. More recently simple two-parameter power-laws have been used to characterize the mass-concentration relation (Dolag et al. 2004; Shaw et al. 2005).

When considering the inner slopes of dark matter halos, a useful generalization of the NFW formula is

$$\rho(r) = \frac{\rho_0}{(\frac{r}{r_s})^\alpha (1 + \frac{r}{r_s})^{3-\alpha}} \quad (4)$$

(e.g., Hernquist 1990; Zhao 1996; Jing & Suto 2000), where the inner slope α is a free parameter. From their initial simulations, Moore et al. (1999) found a steeper central slope than NFW, with $\alpha = 1.5$. For some years, the question of the precise value for the inner slope remained the topic of much debate. However, a consistent view has now emerged in which real dispersion is expected between the inner slopes for individual halos (Klypin et al. 2001; Tasitsiomi et al. 2004) and where typical values for the inner slopes of clusters lie in the range $\alpha \sim 1.1 \pm 0.4$ (Navarro et al. 2004; Diemand et al. 2004, 2005).

In summary, both a tight mass-concentration relation (for recent results see e.g., Shaw et al. 2005) and an inner density slope for dark matter halos in the range $0.7 < \alpha < 1.5$ are central predictions of the CDM paradigm for structure formation.

In this paper we use Chandra X-ray Observatory data to study the mass profiles for 34 of the most massive, dynamically relaxed galaxy clusters known. Such clusters are among the most promising targets with which to check the central CDM predictions, being both dominated by dark matter (e.g., Allen et al. 2004, and references therein) and having a size that allows us to resolve well within the scale radius, even at high redshifts. We employ an analysis method which minimizes the need for priors associated with the use of parameterized models for the X-ray gas density and/or temperature profiles. The restriction to relaxed clusters also minimizes systematic effects associated with e.g. geometry and possible non-thermal pressure support.

Previous X-ray studies have suggested broad agreement with the theoretically predicted mass-concentration relation (Pointecouteau et al. 2005; Zhang 2006; Vikhlinin et al. 2006; Voigt & Fabian 2006), at least at low redshifts. Here, we increase the detail of this comparison and, for the first time, measure both the slope of the mass-concentration relation and its evolution. We show that tension may exist between the Chandra data and some simple models based on CDM simulations for lower mass halos. With regard to the inner density slope, Chandra and XMM-Newton results to date have, in general, suggested good agreement with the CDM predictions (Allen et al. 2001; Schmidt et al. 2001; Allen et al. 2002; Lewis et al. 2002, 2003; Buote & Lewis 2004; Arabadjis et al. 2002; Arabadjis & Bautz 2004; Andersson & Madejski 2004). After some initial controversy, there is also an emerging consensus that strong gravitational lensing data support inner dark matter density slopes of about unity in several clusters (Smith et al. 2001; Gavazzi et al. 2003; Sand et al. 2002, 2004; Bartelmann & Meneghetti 2004; Dalal & Keeton 2003; Meneghetti et al. 2005; Sand et al. 2005). We extend this work and show that the NFW model provides a good description of the total mass and dark matter profiles for most relaxed clusters, rejecting completely the simple singular isothermal model ($\rho \propto 1/r^2$). We also obtain a robust result on the inner slope for the ensemble of clusters.

A flat Λ CDM reference cosmology with $H_0 = 70 \text{ km s}^{-1} \text{ Mpc}^{-1}$ and $\Omega_m = 0.3$ is assumed. In a few cases

cluster masses are quoted with a Hubble constant scale $h = H_0/100 \text{ km s}^{-1} \text{ Mpc}^{-1}$.

2 METHOD

2.1 Target selection

Our target clusters are the most massive, dynamically relaxed clusters known in the redshift range $0 < z < 0.7$. They form a restricted set of the clusters used by Allen et al. (2006, in preparation) to study the evolution of the X-ray gas mass fraction and constrain cosmological parameters. In detail, we have used only the targets from that study for which the temperature is measured in at least four independent bins, which permits reliable measurements on the inner density slopes. The target clusters all have mass weighted X-ray temperatures measured within the radius r_{2500}^1 , $kT_{2500} \gtrsim 5 \text{ keV}$ (Allen et al. 2006, in preparation).

The clusters exhibit a high degree of dynamical relaxation in their Chandra images, with sharp central X-ray surface brightness peaks, regular elliptical X-ray isophotes and minimal isophote centroid variations. The clusters show minimal evidence for departures from hydrostatic equilibrium in X-ray pressure maps (Million et al. , in preparation). The exceptions to this are RXJ1347.5-1145, and MACSJ0744.9+3927, for which clear substructure is observed between position angles of 90-190 degrees and 210-330 degrees, respectively. These regions, associated with obvious substructure, have been excluded from the analysis. The restriction to clusters with the highest possible degree of dynamical relaxation (for which the assumption of hydrostatic equilibrium should be most valid) minimizes systematic scatter and allows the most precise test of the CDM model predictions (e.g., Nagai et al. 2006).

2.2 Observations, data reduction and spectral analysis

The Chandra observations were carried out using the Advanced CCD Imaging Spectrometer (ACIS) between 1999 August 30 and 2005 June 28. The standard level-1 event lists produced by the Chandra pipeline processing were reprocessed using the CIAO (version 3.2.2) software package, including the latest gain maps and calibration products. Bad pixels were removed and standard grade selections applied. Where possible, the extra information available in VFAINT mode was used to improve the rejection of cosmic ray events. The data were cleaned to remove periods of anomalously high background using the standard energy ranges and time bins recommended by the Chandra X-ray Center. The net exposure times after cleaning are summarized in Table 1.

The data have been analysed using techniques discussed by Allen et al. (2004) and references therein. In brief, concentric annular spectra were extracted from the cleaned event lists, centred on the coordinates listed in Table 1. Emission associated with X-ray point sources or obvious substructure (Section 2.1) was excluded. The spectra were analysed using

¹ r_{2500} is the radius within which the mean mass density is 2500 times the critical density of the Universe at the redshift of the cluster.

Table 1. Summary of the Chandra observations. Columns list the target name, redshift, observation date, detector used, observation mode, net exposure after all cleaning and screening processes, and coordinates from the X-ray centres used in the analysis. Where multiple observations of a single target have been used, these are listed separately. Redshifts for the MACS clusters are from Ebeling *et al.* 2006, in preparation, and will appear in full in the published article.

	z	Date	Detector	Mode	Exposure (ks)	R.A. (J2000.)	DEC. (J2000.)
Abell 1795(1)	0.063	2002 Jun 10	ACIS-S	VFAINT	13.2	13 48 52.4	26 35 38
Abell 1795(2)	"	2004 Jan 14	ACIS-S	VFAINT	14.3	"	"
Abell 1795(3)	"	2004 Jan 18	ACIS-I	VFAINT	9.6	"	"
Abell 2029(1)	0.078	2000 Apr 12	ACIS-S	FAINT	19.2	15 10 56.2	05 44 41
Abell 2029(2)	"	2004 Jan 08	ACIS-S	FAINT	74.8	"	"
Abell 2029(3)	"	2004 Dec 17	ACIS-I	VFAINT	9.4	"	"
Abell 478(1)	0.088	2001 Jan 27	ACIS-S	FAINT	39.9	04 13 25.2	10 27 55
Abell 478(2)	"	2004 Sep 13	ACIS-I	VFAINT	7.4	"	"
PKS0745-191(1)	0.103	2001 Jun 16	ACIS-S	VFAINT	17.4	07 47 31.7	-19 17 45
PKS0745-191(2)	"	2004 Sep 24	ACIS-I	VFAINT	9.2	"	"
Abell 1413	0.143	2001 May 16	ACIS-I	VFAINT	64.5	11 55 18.1	23 24 17
Abell 2204(1)	0.152	2000 Jul 29	ACIS-S	FAINT	10.1	16 32 47.2	05 34 32
Abell 2204(2)	"	2004 Sep 20	ACIS-I	VFAINT	8.5	"	"
Abell 383(1)	0.188	2000 Nov 16	ACIS-S	FAINT	18.0	02 48 03.5	-03 31 45
Abell 383(2)	"	2000 Nov 16	ACIS-I	VFAINT	17.2	"	"
Abell 963	0.206	2000 Oct 11	ACIS-S	FAINT	35.8	10 17 03.8	39 02 49
RXJ0439.0+0520	0.208	2000 Aug 29	ACIS-I	VFAINT	7.6	04 39 02.3	05 20 44
RXJ1504.1-0248	0.215	2005 Mar 20	ACIS-I	VFAINT	29.4	15 04 07.9	-02 48 16
RXJ2129.6+0005	0.235	2000 Oct 21	ACIS-I	VFAINT	7.6	21 29 39.9	00 05 20
Abell 1835(1)	0.252	1999 Dec 11	ACIS-S	FAINT	18.0	14 01 01.9	02 52 43
Abell 1835(2)	"	2000 Apr 29	ACIS-S	FAINT	10.3	"	"
Abell 611	0.288	2001 Nov 03	ACIS-S	VFAINT	34.5	08 00 56.8	36 03 24
Zwicky 3146	0.291	2000 May 10	ACIS-I	FAINT	41.4	10 23 39.4	04 11 14
Abell 2537	0.295	2004 Sep 09	ACIS-S	VFAINT	36.0	23 08 22.1	-02 11 29
MS2137.3-2353(1)	0.313	1999 Nov 18	ACIS-S	VFAINT	20.5	21 40 15.2	-23 39 40
MS2137.3-2353(2)	"	2003 Nov 18	ACIS-S	VFAINT	26.6	"	"
MACSJ0242.6-2132	0.314	2002 Feb 07	ACIS-I	VFAINT	10.2	02 42 35.9	-21 32 26
MACSJ1427.6-2521		2002 Jun 29	ACIS-I	VFAINT	14.7	14 27 39.4	-25 21 02
MACSJ2229.8-2756	0.324	2002 Nov 13	ACIS-I	VFAINT	11.8	22 29 45.3	-27 55 37
MACSJ0947.2+7623	0.345	2000 Oct 20	ACIS-I	VFAINT	9.6	09 47 13.1	76 23 14
MACSJ1931.8-2635	0.352	2002 Oct 20	ACIS-I	VFAINT	12.2	19 31 49.6	-26 34 34
MACSJ1115.8+0129		2003 Jan 23	ACIS-I	VFAINT	10.2	11 15 52.1	01 29 53
MACSJ1532.9+3021(1)	0.363	2001 Aug 26	ACIS-S	VFAINT	9.4	15 32 53.9	30 20 59
MACSJ1532.9+3021(2)	"	2001 Sep 06	ACIS-I	VFAINT	9.2	"	"
MACSJ0011.7-1523(1)		2002 Nov 20	ACIS-I	VFAINT	18.2	00 11 42.9	-15 23 22
MACSJ0011.7-1523(2)	"	2005 Jun 28	ACIS-I	VFAINT	32.1	"	"
MACSJ1720.3+3536(1)	0.391	2002 Nov 03	ACIS-I	VFAINT	16.6	17 20 16.8	35 36 27
MACSJ1720.3+3536(2)	"	2005 Nov 22	ACIS-I	VFAINT	24.8	"	"
MACSJ0429.6-0253	0.399	2002 Feb 07	ACIS-I	VFAINT	19.1	04 29 36.1	-02 53 08
MACSJ0159.8-0849(1)		2002 Oct 02	ACIS-I	VFAINT	14.1	01 59 49.4	-08 49 58
MACSJ0159.8-0849(2)	"	2004 Dec 04	ACIS-I	VFAINT	28.9	"	"
MACSJ0329.7-0212(1)	0.450	2002 Dec 24	ACIS-I	VFAINT	16.8	03 29 41.7	-02 11 48
MACSJ0329.7-0212(2)	"	2004 Dec 06	ACIS-I	VFAINT	31.1	"	"
RXJ1347.5-1145(1)	0.451	2000 Mar 03	ACIS-S	VFAINT	8.6	13 47 30.6	-11 45 10
RXJ1347.5-1145(2)	"	2000 Apr 29	ACIS-S	FAINT	10.0	"	"
RXJ1347.5-1145(3)	"	2003 Sep 03	ACIS-I	VFAINT	49.3	"	"
3C295(1)	0.461	1999 Aug 30	ACIS-S	FAINT	15.4	14 11 20.5	52 12 10
3C295(2)	"	2001 May 18	ACIS-I	FAINT	72.4	"	"
MACSJ1621.6+3810(1)	0.461	2002 Oct 18	ACIS-I	VFAINT	7.9	16 21 24.8	38 10 09
MACSJ1621.6+3810(2)	"	2004 Dec 11	ACIS-I	VFAINT	32.2	"	"
MACSJ1621.6+3810(3)	"	2004 Dec 25	ACIS-I	VFAINT	26.1	"	"
MACSJ1311.0-0311	0.494	2005 Apr 20	ACIS-I	VFAINT	56.2	13 11 01.6	-03 10 40
MACSJ1423.8+2404	0.539	2003 Aug 18	ACIS-S	VFAINT	113.5	14 23 47.9	24 04 43
MACSJ0744.9+3927(1)	0.686	2001 Nov 12	ACIS-I	VFAINT	17.1	07 44 52.9	39 27 27
MACSJ0744.9+3927(2)	"	2003 Jan 04	ACIS-I	VFAINT	15.6	"	"
MACSJ0744.9+3927(3)	"	2004 Dec 03	ACIS-I	VFAINT	41.3	"	"

XSPEC (version 11.3: Arnaud 1996), the MEKAL plasma emission code (Kaastra & Mewe 1993; incorporating the Fe-L calculations of Liedahl et al. 1995) and the photoelectric absorption models of Balucinska-Church & McCammon (1992). We have included standard correction factors to account for time-dependent contamination along the instrument light path. In addition, we have incorporated a small correction to the High Resolution Mirror Assembly model in CIAO 3.2.2, which takes the form of an 'inverse' edge with an energy, $E=2.08$ keV and optical depth $\tau = -0.1$ (H. Marshall, private communication) and boosted the overall effective area by six per cent, to better match later calibration data (A. Vikhlinin, private communication). Only data in the 0.8 – 7.0 keV energy range were used in the analysis (the exceptions being the earliest observations of 3C 295, Abell 1835 and Abell 2029 where a wider 0.6 to 7.0 keV band was used).

For the nearer clusters ($z < 0.3$), background spectra were extracted from the blank-field data sets available from the Chandra X-ray Center. These were cleaned in an identical manner to the target observations. In each case, the normalizations of the background files were scaled to match the count rates in the target observations measured in the 9.5–12 keV band. Where required, *e.g.* due to the presence of strong excess soft emission in the field of Abell 2029, a spectral model for any unusual soft background emission was included in the analysis. For the more distant systems (as well as for the first observation of Abell 1835, the ACIS-I observation of Abell 383, and the observations of Abell 2537, RXJ 2129.6+0005 and Zwicky 3146) background spectra were extracted from appropriate, source free regions of the target data sets. (We have confirmed that similar results are obtained using the blank-field background data sets.) In order to minimize systematic uncertainties and due to the specific goals of this work, we have restricted our spectral analysis to radii within which systematic uncertainties in the background subtraction (established by the comparison of different background subtraction methods) are smaller than the statistical uncertainties in the results. All results are drawn from spectral analyses limited to ACIS chips 0,1,2,3 and 7 which have the most accurate calibration, although ACIS chip 5 was also used to study the soft X-ray background in ACIS-S observations. We do not attempt to extend our analyses to larger radii using the data from other chips.

Separate photon-weighted response matrices and effective area files were constructed for each region using calibration files appropriate for the period of observations. The spectra for all annuli for a given cluster were modelled simultaneously in order to determine the deprojected X-ray gas temperature and metallicity profiles, under the assumption of spherical symmetry.

2.3 Cluster mass profile measurements

2.3.1 Basics of the mass analysis

Under the assumptions of hydrostatic equilibrium and spherical symmetry, the observed X-ray surface brightness profile and the deprojected X-ray gas temperature profile may together be used to determine the X-ray emitting gas mass and total mass profile of a galaxy cluster. For this analysis, we have used an enhanced version of the Cambridge

X-ray deprojection code described by *e.g.* White, Jones & Forman (1997). This method is particularly well suited to the present study in that it does not require approximate fitting functions for the X-ray temperature, gas density or surface brightness when measuring the total, gravitating mass². The use of such functions introduces priors into an analysis which can complicate the interpretation of results and, in particular, the estimation of measurement errors.

We have carried out two separate mass analyses: firstly (method 1) an analysis in which the total mass profile (dark plus luminous matter) was modelled using either an NFW or singular isothermal sphere. Detailed results on the X-ray emitting gas profiles were also determined at this stage. Secondly (method 2) an analysis in which we separated the total mass profile into three parts: the dark matter halo (fitted with a generalized NFW profile), the X-ray emitting gaseous halo (approximated, for the purposes of this analysis only, with a beta model), and the optically luminous mass of the cD galaxy (approximated with a Jaffe or de Vaucouleurs model).

The normalization, ρ_0 , of the generalized NFW mass model (eq. 4) is usually written as

$$\rho_0 = \rho_{\text{crit}} \delta_c \quad (5)$$

where

$$\rho_{\text{crit}} = 3H(z)^2 / 8\pi G \quad (6)$$

is the critical density at the redshift z of the cluster. G is the gravitational constant and the Hubble parameter $H(z)$ is defined by

$$H(z)^2 = H_0^2 (1+z)^2 (1+z\Omega_m + \frac{\Omega_\Lambda}{(1+z)^2} - \Omega_\Lambda). \quad (7)$$

Here Ω_m is the matter density and Ω_Λ is the vacuum-energy density of the Universe in units of the critical density.

The amplitude δ_c depends only on the concentration parameter $c = \frac{r_s}{r_{200}}$ (r_{200} is the radius within which the average mass density is 200 times ρ_{crit}). For convenient computation, δ_c can be written using the Gauss hypergeometric function $F(a,b;c;z)$ (Abramowitz & Stegun 1965)

$$\Phi(y) = \frac{y^{3-\alpha}}{3-\alpha} F(3-\alpha, 3-\alpha; 4-\alpha; -y) \quad (8)$$

as

$$\delta_c = \frac{200}{3} \frac{c^3}{\Phi(c)} \quad (9)$$

(Wyithe et al. 2001). For the original NFW mass model with $\alpha = 1$, one obtains $\Phi(c) = \ln(1+c) - c/(1+c)$ (Navarro et al. 1996).

With mass analysis method 2, in which the dark and dominant baryonic matter components were separated, the X-ray emitting gas distribution was approximated using a beta-model (Cavaliere & Fusco-Femiano 1978)

$$\rho_{\text{gas}}(r) = \rho_{0,\text{gas}} \left[1 + \left(\frac{r}{r_{c,\text{gas}}} \right)^2 \right]^{-\frac{3\beta}{2}}, \quad (10)$$

² As discussed in the text, priors are required when modelling the dark matter and X-ray and optically luminous matter components separately

where $\rho_{0,\text{gas}}$ is the central gas density, $r_{c,\text{gas}}$ is the core radius of the gas profile and β is the slope parameter. (We stress that detailed results on the X-ray emitting gas profiles, used for example in the measurement of cluster gas mass fractions, are determined with method 1 and involve no assumption about the functional form of the gas profile. The use of the beta-model with method 2 provides a convenient approximation, when recovering the dark matter profiles. Although the beta model does not provide a precise match to the X-ray gas mass distribution in all cases, the systematic uncertainties in the dark matter profiles that result from its use are small, primarily because the X-ray emitting gas contributes only ~ 12 per cent of the total mass; Allen *et al.* 2006, in preparation).

All of the target clusters have a single, optically dominant galaxy at their centres. With method 2, we accounted for the mass of stars in the central galaxy using a Jaffe (1983) model (Sand *et al.* 2002, 2004). This was added to the generalized NFW potential for the dark matter halo and the beta-model for the X-ray emitting gas. The Jaffe (1983) model is

$$\rho_J(r) = \frac{\rho_{0,J}}{(\frac{r}{r_c})^2(1 + \frac{r}{r_c})^2} \quad (11)$$

with central density $\rho_{0,J}$ and core radius r_c . The total mass for the model is finite, $M_J = 4\pi r_c^3 \rho_{0,J}$. Since including this model into the analysis has only a small effect on the results (Section 4.2) but requires two parameters, we chose to fix these two parameters to sensible values. We adopt $R_e = 0.76 r_c = 25$ kpc as a typical effective radius (e.g., Sand *et al.* 2002, 2005). For the well-studied cD galaxy in MS2137-2353, Sand *et al.* (2002) measure a total V-band luminosity of $L_V = 4.16 \times 10^{11} L_\odot$. Using the M/L_V relation of Fukugita *et al.* (1998)

$$\frac{M}{L_V} = 4.0 + 0.38(t_g - 10 \text{ Gyr}), \quad (12)$$

where t_g is the age of the galaxy (we assume a formation redshift $z_f = 2.0$), we estimate the total stellar mass associated with the cD galaxy of $1.14 \times 10^{12} M_\odot$. The central galaxy for each cluster in the sample is assumed to have a similar stellar mass.

We have also carried out a repeat analysis in which the Jaffe (1983) model for the stellar mass associated with the central, dominant galaxies was replaced by a de Vaucouleurs (1948) model. This analytical model is described by the surface mass density

$$\Sigma(r) = \Sigma_e e^{-7.67[(r/R_e)^{1/4} - 1]}, \quad (13)$$

where Σ_e is the surface density at the effective (or half-mass) radius R_e . The 3-dimensional mass profile of the de Vaucouleurs model was calculated by Young (1976) and has a shallower central slope close to unity. However, similar results on the cluster dark matter profiles were obtained in all cases, showing that the precise choice of the galaxy model has a negligible effect on the results.

2.3.2 Best-fitting values and confidence limits

Given the observed surface brightness profile and a particular parameterized mass model, the deprojection code is used to predict the temperature profile of the X-ray gas. This

Table 2. Regions with residual substructure that were down-weighted in the mass analysis. A systematic uncertainty of ± 30 per cent has been added in quadrature to all temperature measurements made within radii R_{sub} .

R_{sub} (kpc)	
Abell 1795	73.3
Abell 2029	30.0
Abell 478	14.6
PKS0745-191	53.0
Abell 1413	38
Abell 2204	76.8
Abell 383	38.7
RXJ1504.1-0248	79.1
RXJ2129.6+0005	40.4
Zwicky 3146	242
Abell 2537	41.1
MACSJ2229.8-2756	42.0
MACSJ0947.2+7623	40.1
MACSJ1931.8-2635	41.5
MACSJ1115.8+0129	83.4
MACSJ1532.9+3021	42.3
MACSJ1621.6+3810	43.1

model temperature profile is compared with the observed spectral, deprojected temperature profile and the goodness of fit is calculated using the sum over all temperature bins

$$\chi^2 = \sum_{\text{all bins}} \left(\frac{T_{\text{obs}} - T_{\text{model}}}{\sigma_{\text{obs}}} \right)^2, \quad (14)$$

where T_{obs} is the observed, spectral deprojected temperature profile and T_{model} is the model, rebinned to the same spatial scale using flux weighting.³

For each mass model, we determine the best-fitting parameter values and uncertainties via χ^2 minimization. We use the LEASQR Levenberg-Marquardt routine (Marquardt 1963) from the GNU Octave Repository, available online at <http://sourceforge.net>. (A full Monte Carlo analysis, as described above, is run for each set of parameter values examined in the minimization procedure.)

For a number of the clusters, the Chandra images indicate small levels of residual substructure in the innermost regions, which probably result from ‘sloshing’ of the X-ray emitting gas within the central potentials (e.g., Markevitch *et al.* 2001; Ascasibar & Markevitch 2006; Allen *et al.* 1992) and/or interactions between central radio sources and the surrounding intracluster gas (e.g., Böhringer *et al.* 1993; Fabian *et al.* 2000, 2003, 2006; Birzan *et al.* 2004; Dunn & Fabian 2004; Forman *et al.* 2005; Dunn *et al.* 2005; Rafferty *et al.* 2006; Allen *et al.* 2006). The regions affected by such substructure are listed in Table 2. A systematic uncertainty of ± 30 per cent has been added in quadrature to the spec-

³ In detail, we use the median model temperature profile determined from 100 Monte-Carlo simulations. The outermost pressure, at the limit of the X-ray surface brightness profile, is fixed using an iterative method that ensures a smooth, power law pressure gradient in these regions. The model temperature profiles, for radii spanned by the spectral data, are not sensitive to reasonable choices for the outer pressures.

tral results from these regions which leads to them having little weight in the mass analysis.

3 RESULTS

3.1 Total mass profiles: NFW versus singular isothermal sphere

Table 3.1 summarizes the results from the initial mass analysis (method 1) in which the total mass profiles (dark-plus-luminous matter) were modelled using either an NFW (inner slope $\alpha = 1$ fixed) or singular isothermal sphere model ($\rho(r) = A/r^2$, with the normalization A free). We see that for most clusters the NFW model provides a reasonable description of the total mass profiles. For 27 out of 34 clusters, the χ^2/DOF value has a probability of 0.05 or better and only for Abell 383 and 1413 does the probability drop below 0.001. In contrast, the singular isothermal sphere model can be firmly rejected for most clusters in the sample.

Combining the results for all clusters, the NFW model gives a total χ^2 of 171.0 for 95 degrees of freedom (DOF) (with Abell 383 and 1413 contributing a total χ^2 of 47.9). The singular isothermal sphere gives $\chi^2 = 3031.1$ for 129 DOF, indicating an extremely low model probability.

3.2 Dark matter profiles. The NFW model and mass-concentration relation

Table 4 summarizes the results from the analysis with method 2, in which the cluster mass distributions were separated into three parts: the dark matter halo (fitted with a generalized NFW profile), the X-ray emitting gaseous halo (approximated with a beta model), and the optically luminous mass of the central dominant galaxy (approximated with a Jaffe or a de Vaucouleurs model). In the first case, we examined models in which the inner slope of the dark matter profile was fixed at $\alpha = 1$ i.e. the standard NFW model.

Our first conclusion is that, as with the analysis of the total mass profiles, the NFW model provides a good overall description of the dark matter profiles in the clusters. For 27 out of 34 clusters, the χ^2/DOF value has a probability of 0.05 or better and only for Abell 383 and 1413 does the model fail significantly. Combining the results for all clusters, the NFW model gives a total χ^2 of 176.1 for 95 degrees of freedom (DOF) (with Abell 383 and 1413 contributing a total χ^2 of 48.0; note that the inclusion of the separate mass components for the X-ray emitting gas and stars introduces no additional free parameters in the fits.) The concentration parameters, c for the dark matter profiles are slightly lower, and the scale radii slightly higher, than for the total matter distributions. However, in general the results are quite similar.

As discussed in Section 1, one of the central predictions from simulations of CDM halos is the mass-concentration relation. In order to allow for the most direct comparison with theory, we have used the values in Table 4 to calculate the concentration parameters c_{vir} and masses M_{vir} measured within the virial radii for the clusters. We adopt the definitions of virial radius and virial mass used by Shaw et al. (2005)

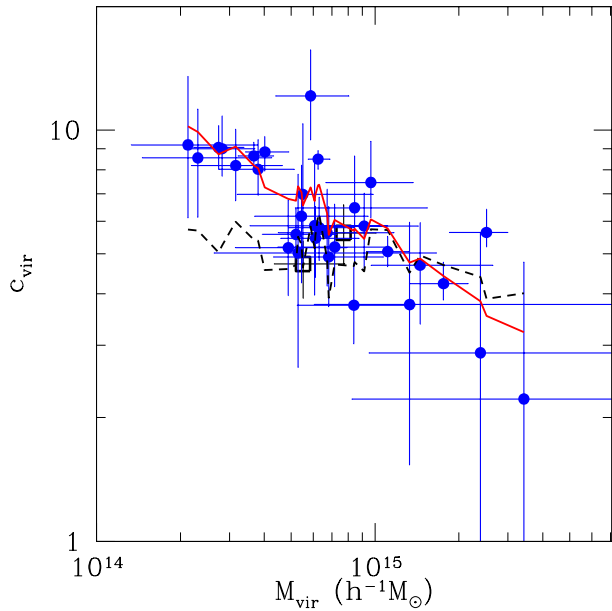


Figure 1. The virial mass-concentration relation for the dark matter halos. The solid line shows the best-fitting model with $c_0 = 6.90 \pm 0.77$, $a = -0.41 \pm 0.11$ and $b = 0.54 \pm 0.47$ (95 per cent confidence limits). The dashed line shows the prediction from the CDM simulations of Shaw et al. (2005), with $c_0 = 6.47$, $a = -0.12$ and $b = 1.0$ fixed. The two clusters for which the NFW model fails to provide a reasonable description of the Chandra data, Abell 383 and 1413, are plotted with open square symbols and have been excluded from the fits.

$$M_{\text{vir}} = \frac{4}{3} \pi r_{\text{vir}}^3 \Delta_c(z) \rho_{\text{crit}}(z), \quad (15)$$

where the virial overdensity is given by $\Delta_c = 178 \Omega_m(z)^{0.45}$. Note that the translation between c (as listed in Table 4) and c_{vir} must be done separately for each cluster, due to the inherent redshift dependence. The virial concentration parameter is defined in the usual manner as $c_{\text{vir}} = r_{\text{vir}}/r_s$. Table 5 lists the results on c_{vir} and M_{vir} for the dark matter halos using the standard NFW model ($\alpha = 1$).

Fig. 1 shows the variation of c_{vir} with M_{vir} measured from the Chandra data. A tight relation is observed with a clear trend for decreasing concentration parameter with increasing mass.

The literature contains a variety of simple analytical forms to describe the expected form of the mass-concentration relation, based on CDM numerical simulations. The simplest of these is a power-law model (Dolag et al. 2004)

$$c_{\text{vir}}(z) = \frac{c_0}{1+z} \left(\frac{M_{\text{vir}}}{8 \times 10^{14} h^{-1} M_\odot} \right)^a. \quad (16)$$

Shaw et al. (2005) present one of the largest statistical studies of cluster-sized CDM halos to date. Fitting a $z = 0.05$ snapshot of their simulated data with the Dolag et al. (2004) power law model, these authors find $c_0 = 6.47 \pm 0.03$ and $a = -0.12 \pm 0.03$ (68 per cent confidence limits). The dashed line in Fig. 1 shows the model defined by these parameters, overlaid on the Chandra results. The model clearly provides a poor fit to the observations, $\chi^2 = 124.9$ for 30 DOF, lying

Table 3. Results from fits to the total mass profiles with NFW (slope $\alpha = 1$ fixed) and singular-isothermal (SI) models (analysis method 1). Columns list the number of temperature bins used in the analysis of each cluster, the scale radius r_s (in kpc) and concentration parameter $c = r_{200}/r_s$ for the NFW models, and the goodness of fit (χ^2/DOF) for both models. The SI model provides a poor description of the data. Quoted uncertainties are 68 per cent ($\Delta\chi^2 = 1.0$) confidence limits.

	Number of kT bins	TOTAL MASS (LUMINOUS PLUS DARK MATTER)			
		r_s	NFW MODEL c	χ^2/DOF	SI MODEL χ^2/DOF
Abell 1795	5	$0.41^{+0.14}_{-0.07}$	$4.62^{+0.65}_{-0.79}$	1.67/3	49.2/4
Abell 2029	6	$0.27^{+0.05}_{-0.02}$	$7.06^{+0.26}_{-0.74}$	4.94/4	303/5
Abell 478	7	$0.50^{+0.06}_{-0.07}$	$4.47^{+0.45}_{-0.28}$	8.88/5	615/6
PKS0745-191	7	$0.35^{+0.13}_{-0.09}$	$6.24^{+1.38}_{-1.10}$	5.17/5	42.1/6
Abell 1413	6	$0.51^{+0.11}_{-0.12}$	$4.18^{+0.83}_{-0.51}$	24.6/5	91.5/6
Abell 2204	5	$0.19^{+0.09}_{-0.05}$	$9.74^{+2.31}_{-2.25}$	4.41/3	16.6/4
Abell 383	5	$0.48^{+0.12}_{-0.12}$	$3.75^{+0.71}_{-0.48}$	23.3/4	90.0/5
Abell 963	5	$0.40^{+0.12}_{-0.11}$	$4.61^{+1.07}_{-0.73}$	6.19/3	97.8/4
RXJ0439.0+0521	4	$0.19^{+0.06}_{-0.05}$	$7.69^{+1.52}_{-1.29}$	0.30/2	28.3/3
RXJ1504.1-0248	5	$0.54^{+0.29}_{-0.15}$	$4.38^{+1.06}_{-1.05}$	0.91/3	28.1/4
RXJ2129.6+0005	5	$0.38^{+0.45}_{-0.17}$	$4.59^{+2.18}_{-1.84}$	1.53/3	14.7/4
Abell 1835	5	$0.58^{+0.08}_{-0.10}$	$4.20^{+0.52}_{-0.31}$	12.5/3	302/4
Abell 611	5	$0.33^{+0.19}_{-0.12}$	$5.32^{+1.86}_{-1.49}$	2.35/3	25.7/4
Zwicky 3146	5	$0.99^{+5.0}_{-0.58}$	$2.71^{+2.38}_{-2.71}$	0.79/3	11.4/4
Abell 2537	5	$0.36^{+0.37}_{-0.12}$	$4.97^{+1.52}_{-1.87}$	3.30/3	22.2/4
MS2137.3-2353	6	$0.18^{+0.02}_{-0.02}$	$8.08^{+0.81}_{-0.45}$	5.55/4	235/5
MACSJ0242.6-2132	4	$0.18^{+0.02}_{-0.01}$	$7.97^{+0.85}_{-1.12}$	2.93/2	62.1/3
MACSJ1427.6-2521	4	$0.16^{+0.06}_{-0.06}$	$8.08^{+2.62}_{-1.87}$	4.78/2	18.1/3
MACSJ2229.8-2756	4	$0.15^{+0.10}_{-0.05}$	$8.43^{+3.00}_{-2.55}$	1.60/2	6.8/3
MACSJ0947.2+7623	4	$0.31^{+0.19}_{-0.10}$	$6.15^{+1.75}_{-1.58}$	2.56/2	23.6/3
MACSJ1931.8-2635	4	$0.51^{+0.94}_{-0.19}$	$4.05^{+1.42}_{-1.91}$	1.98/2	33.6/3
MACSJ1115.8+0129	4	$1.35^{+5.0}_{-0.91}$	$2.15^{+2.20}_{-2.15}$	1.24/2	13.7/3
MACSJ1532.9+3021	5	$0.33^{+0.17}_{-0.08}$	$5.36^{+1.18}_{-1.19}$	1.77/3	41.8/4
MACSJ0011.7-1523	4	$0.49^{+0.16}_{-0.14}$	$3.75^{+0.83}_{-0.62}$	6.75/2	168/3
MACSJ1720.3+3536	4	$0.33^{+0.14}_{-0.08}$	$5.21^{+0.98}_{-1.00}$	1.19/2	49.8/3
MACSJ0429.6-0253	4	$0.16^{+0.04}_{-0.04}$	$8.46^{+1.32}_{-1.07}$	1.87/2	25.8/3
MACSJ0159.8-0849	4	$0.35^{+0.12}_{-0.08}$	$5.49^{+0.97}_{-0.86}$	4.45/2	52.9/3
MACSJ0329.7-0212	4	$0.29^{+0.07}_{-0.05}$	$5.48^{+0.62}_{-0.62}$	6.24/2	86.0/3
RXJ1347.5-1144	6	$0.45^{+0.11}_{-0.07}$	$5.63^{+0.64}_{-0.67}$	16.1/4	257/5
3C295	4	$0.15^{+0.02}_{-0.03}$	$8.64^{+1.05}_{-0.85}$	1.12/2	61.3/3
MACSJ1621.6+3810	4	$0.25^{+0.18}_{-0.10}$	$6.51^{+2.57}_{-2.04}$	4.01/2	17.6/3
MACSJ1311.0-0311	4	$0.31^{+0.15}_{-0.09}$	$4.91^{+1.28}_{-1.10}$	1.55/2	25.4/3
MACSJ1423.8+2404	4	$0.17^{+0.03}_{-0.02}$	$8.27^{+0.89}_{-0.74}$	0.07/2	74.1/3
MACSJ0744.9+3927	4	$0.32^{+0.19}_{-0.08}$	$4.88^{+1.03}_{-1.30}$	4.40/2	40.9/3

systematically below the data at lower masses and above it in the highest mass range. Note that the two clusters for which the NFW model provides a formally unacceptable description of the Chandra data, Abell 383 and 1413, have been excluded from the fit and are plotted with open square symbols.

One should remember that the Chandra observations reported here are for the most massive, dynamically relaxed clusters known within $z < 0.7$. (Our targets represent the most relaxed ~ 20 per cent of clusters in this mass and redshift range.) We have, therefore, also determined the best-fitting power-law parameters appropriate for the most relaxed 20 per cent of simulated halos with $M_{\text{vir}} > 2 \times 10^{14} h^{-1} M_{\odot}$ in the Shaw et al. (2005) study. (In detail, this is done by selecting only those clusters with a substructure fraction, as defined by those authors, $f_s < 0.045$). The resulting power-law fit parameters are

$c_0 = 6.8$ and $a = -0.16$. Although giving slightly better agreement with the observations, this model still provides a poor description of the Chandra data with $\chi^2 = 100.15$ for 30 DOF.

Physical motivation for the power-law model and its $(1+z)^{-1}$ redshift dependence is presented by Bullock et al. (2001). In their model they assume that the ratio of the virial mass, M_{vir} , to the volume inside the scale radius, V_s , is proportional to the matter density $\rho_m(z_{\text{coll}})$ at the redshift, z_{coll} , when the cluster formed:

$$\rho_m(z_{\text{coll}}) \propto \frac{M_{\text{vir}}}{V_s} \propto \frac{\rho_m r_{\text{vir}}^3}{r_s^3} = \rho_m c_{\text{vir}}^3. \quad (17)$$

Since the matter density ρ_m was larger in the past, $\rho_m \propto (1+z)^3$, the typical concentration parameter for a halo of mass M_{vir} is smaller at higher redshifts, $c_{\text{vir}} \propto (1+z)^{-1}$. Bullock et al. (2001) associate each redshift with a typical

Table 4. Results on the dark matter profiles for the clusters, from the fits including separate components for the X-ray emitting gas and dominant cluster galaxy (analysis method 2). For the standard NFW model (inner slope $\alpha = 1$ fixed) we list the scale radius r_s (in kpc) and concentration parameter $c = r_{200}/r_s$. For the generalized NFW model, we give results on the inner slope α . Only inner slopes in the range $0 < \alpha < 1.8$ were examined; where confidence limits are absent in the table, the fit results were consistent with the allowed limits for α . For both models, we list the results on the goodness of fit (χ^2/DOF). Quoted uncertainties are 68 per cent ($\Delta\chi^2 = 1.0$) confidence limits.

	DARK MATTER PROFILES				
	NFW ($\alpha = 1$)		χ^2/DOF	GENERALIZED NFW	
	r_s	c		α	χ^2/DOF
Abell 1795	$0.41^{+0.13}_{-0.09}$	$4.45^{+0.85}_{-0.77}$	2.21/3	$0.00^{+1.24}$	1.65/2
Abell 2029	$0.28^{+0.03}_{-0.02}$	$6.63^{+0.34}_{-0.37}$	4.47/4	$1.16^{+0.22}_{-0.34}$	4.31/3
Abell 478	$0.56^{+0.09}_{-0.08}$	$3.91^{+0.36}_{-0.33}$	6.90/5	$1.10^{+0.12}_{-0.21}$	6.66/4
PKS0745-191	$0.36^{+0.13}_{-0.11}$	$5.85^{+1.55}_{-1.07}$	5.26/5	$0.78^{+0.64}_{-0.64}$	5.17/4
Abell 1413	$0.43^{+0.14}_{-0.09}$	$4.43^{+0.78}_{-0.75}$	24.5/5	$1.54^{+0.06}_{-0.21}$	22.0/4
Abell 2204	$0.18^{+0.08}_{-0.05}$	$9.75^{+2.92}_{-2.17}$	4.93/3	$0.00^{+0.88}$	3.62/2
Abell 383	$0.45^{+0.16}_{-0.08}$	$3.76^{+0.53}_{-0.68}$	23.5/4	$0.00^{+0.40}$	20.1/2
Abell 963	$0.40^{+0.16}_{-0.10}$	$4.38^{+0.88}_{-0.88}$	7.21/3	$0.00^{+0.54}$	4.55/2
RXJ0439.0+0521	$0.21^{+0.08}_{-0.06}$	$6.65^{+1.54}_{-1.21}$	0.62/2	$0.00^{+1.21}$	0.04/1
RXJ1504.1-0248	$0.62^{+0.43}_{-0.49}$	$3.76^{+1.05}_{-1.09}$	0.88/3	$0.92^{+0.61}_{-0.61}$	0.87/2
RXJ1219.6+0005	$0.41^{+0.72}_{-0.20}$	$4.06^{+2.31}_{-1.97}$	1.51/3	$1.08^{+0.52}_{-1.08}$	1.49/2
Abell 1835	$0.71^{+0.12}_{-0.14}$	$3.42^{+0.45}_{-0.31}$	14.2/3	$0.00^{+0.76}$	11.3/2
Abell 611	$0.32^{+0.24}_{-0.11}$	$5.08^{+1.72}_{-1.62}$	2.43/3	$0.64^{+0.94}_{-0.94}$	2.37/2
Zwicky 3146	$1.14^{+>5.0}_{-0.71}$	$2.31^{+2.31}_{-2.31}$	0.82/3	$0.00^{+1.51}$	0.63/2
Abell 2537	$0.35^{+0.28}_{-0.15}$	$4.82^{+2.32}_{-1.59}$	2.74/3	$0.00^{+1.04}$	1.82/2
MS2137.3-2353	$0.20^{+0.03}_{-0.02}$	$7.21^{+0.57}_{-0.59}$	5.10/4	$1.00^{+0.25}_{-0.35}$	5.10/3
MACSJ0242.6-2132	$0.22^{+0.06}_{-0.05}$	$6.68^{+1.23}_{-0.92}$	3.01/2	$0.66^{+0.65}_{-0.65}$	2.88/1
MACSJ1427.6-2521	$0.17^{+0.12}_{-0.06}$	$7.14^{+2.29}_{-2.05}$	4.92/2	$0.00^{+1.58}$	4.66/1
MACSJ2229.8-2756	$0.16^{+0.13}_{-0.07}$	$7.70^{+3.66}_{-2.62}$	1.50/2	$1.68^{+0.15}_{-0.15}$	1.02/1
MACSJ0947.2+7623	$0.35^{+0.24}_{-0.13}$	$5.40^{+1.86}_{-1.51}$	2.66/2	$0.00^{+1.22}$	2.06/1
MACSJ1931.8-2635	$0.69^{+2.46}_{-0.36}$	$3.11^{+1.87}_{-1.88}$	1.88/2	$1.16^{+0.36}_{-0.36}$	1.86/1
MACSJ1115.8+0129	$1.61^{+>5.0}_{-1.14}$	$1.80^{+2.17}_{-1.80}$	1.30/2	$0.00^{+1.36}$	1.03/1
MACSJ1532.9+3021	$0.37^{+0.23}_{-0.12}$	$4.70^{+1.32}_{-1.24}$	2.01/3	$0.00^{+1.16}$	1.36/2
MACSJ0011.7-1523	$0.59^{+0.25}_{-0.19}$	$3.11^{+0.84}_{-0.62}$	8.34/2	$0.00^{+0.41}$	4.57/1
MACSJ1720.3+3536	$0.40^{+0.18}_{-0.13}$	$4.36^{+1.21}_{-0.88}$	1.12/2	$1.08^{+0.38}_{-0.38}$	1.09/1
MACSJ0429.6-0253	$0.17^{+0.05}_{-0.04}$	$7.64^{+1.57}_{-1.10}$	1.41/2	$1.44^{+0.23}_{-0.66}$	0.79/1
MACSJ0159.8-0849	$0.38^{+0.18}_{-0.10}$	$4.93^{+1.01}_{-1.06}$	3.65/2	$1.44^{+0.07}_{-0.22}$	1.60/1
MACSJ0329.7-0212	$0.32^{+0.07}_{-0.07}$	$4.74^{+0.75}_{-0.78}$	6.80/2	$0.00^{+0.86}$	5.43/1
RXJ1347.5-1144	$0.54^{+0.08}_{-0.11}$	$4.79^{+0.68}_{-0.38}$	18.0/4	$0.00^{+0.40}$	10.1/3
3C295	$0.16^{+0.03}_{-0.03}$	$7.78^{+1.03}_{-0.90}$	1.71/2	$0.00^{+1.05}$	0.86/1
MACSJ1621.6+3810	$0.26^{+0.21}_{-0.11}$	$5.97^{+2.95}_{-1.95}$	4.12/2	$0.00^{+1.53}$	3.94/1
MACSJ1311.0-0311	$0.33^{+0.18}_{-0.11}$	$4.42^{+1.39}_{-1.06}$	1.46/2	$1.46^{+0.13}_{-1.08}$	0.94/1
MACSJ1423.8+2404	$0.18^{+0.03}_{-0.02}$	$7.68^{+0.71}_{-0.79}$	0.19/2	$0.66^{+0.62}_{-0.62}$	0.02/1
MACSJ0744.9+3927	$0.36^{+0.19}_{-0.13}$	$4.31^{+1.43}_{-1.06}$	4.72/2	$0.00^{+0.79}$	3.21/1

collapsing mass (defined as a fraction F of the final halo mass) through a critical value of the variance $\sigma(z, M)$ of the density fluctuations. Since $\sigma(M)$ for a Λ CDM model is a power-law for masses $M_{\text{vir}} \lesssim 10^{13} M_{\odot}/F$, this model yields a power-law for the mass-concentration relation (up to this mass scale) with two free parameters. Bullock et al. (2001) suggest $F = 0.01$ (although $F = 0.001$ is also used in the literature). At the high-mass end, $M_{\text{vir}} > 10^{13} M_{\odot}/F$, the model predicts a change in the power-law slope but, unfortunately, also becomes unrealistic as the linear evolution of density fluctuations stalls in the Λ CDM model, preventing high-mass clusters from forming (Bullock et al. 2001; Kuhlen et al. 2005).

Although the Bullock et al. (2001) model and the power law model of Dolag et al. (2004) are attractive in terms of

their simplicity, the limitations of such models for describing the detailed properties of cluster halos should not be overlooked. Firstly, real clusters contain X-ray emitting gas and stars, as well as dark matter. CDM-only simulations do not include cooling and feedback processes which affect the baryonic mass components and modify the overall mass distributions. Secondly, to date, studies of the mass-concentration relation have included very few halos at the largest mass range spanned by the Chandra data; e.g., Shaw et al. (2005) have only a single cluster with $M_{\text{vir}} > 10^{15} h^{-1} M_{\odot}$. Finally, Zhao et al. (2003) argue that at the highest masses, the Bullock et al. (2001) model may over-predict the evolution of c_{vir} with redshift.

Motivated by such considerations, we have introduced additional freedom into the power law model of Dolag et al.

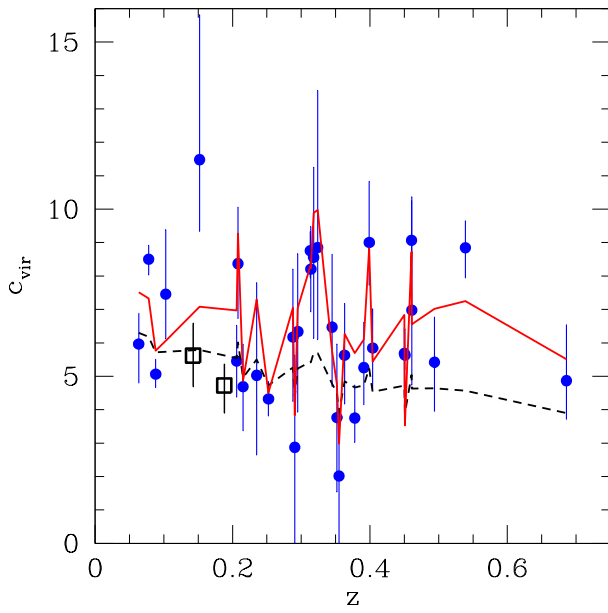


Figure 2. The measured concentration parameters for the dark matter halos as a function of redshift. The solid line shows the best-fitting model with $c_0 = 6.90 \pm 0.77$, $a = -0.41 \pm 0.11$ and $b = 0.54 \pm 0.47$ (95 per cent confidence limits). The dashed line shows the prediction from the CDM simulations of Shaw et al. (2005) with $c_0 = 6.47$, $a = -0.12$ and $b = 1.0$. The apparent absence of redshift evolution in the data may be an artifact induced by the steep slope of the underlying mass-concentration relation (see text for details). Symbols as in Fig. 1

(2004). As well as having c_0 and a as free fit parameters, we also allow the redshift evolution to evolve as $(1+z)^{-b}$, with b free.

$$c = \frac{c_0}{(1+z)^b} \left(\frac{M_{\text{vir}}}{8 \times 10^{14} h^{-1} M_{\odot}} \right)^a. \quad (18)$$

The results from a fit with this model, with c_0 , a and b all free, are shown by the solid line in Fig. 1. The model provides a significantly improved description of the data with $\chi^2 = 43.7$ for 29 degrees of freedom and best-fitting parameters $c_0 = 6.90 \pm 0.77$, $a = -0.41 \pm 0.11$ and $b = 0.54 \pm 0.47$ (95 per cent confidence limits; similar results are obtained from a Monte Carlo analysis of the $(c_{\text{vir}}|M_{\text{vir}})$ data wherein the results for individual clusters are scattered according to their measurement errors). Although the normalization, c_0 , is consistent with the Shaw et al. (2005) simulations and Dolag et al. (2004) model, the redshift evolution is marginally slower and the slope of the mass-concentration relation is noticeably steeper.

Fig. 2 shows the variation of concentration parameter with redshift. At low redshifts, the fit to the Shaw et al. (2005) simulated data with the Dolag et al. (2004) model ($c_0 = 6.47$, $a = -0.12$, $b = 1$) provides a reasonable match to the data (in agreement with the conclusions drawn by Pointecouteau et al. 2005; Zhang 2006; Vikhlinin et al. 2006; Voigt & Fabian 2006). At higher redshifts, however, the observed c_{vir} values exceed the Shaw et al. (2005) model predictions. The most striking feature of Fig. 2 is an apparent absence of redshift evolution in the concentration parame-

ter. Indeed, when fixing the slope parameter a to the Shaw et al. (2005) value of $a = -0.12$, a fit with c_0 and b free gives a redshift evolution parameter $b = 0.20 \pm 0.45$ (95 per cent confidence limits), consistent with no evolution or even positive evolution of c_{vir} with M_{vir} . However, note that the χ^2 for this fit is significantly worse ($\chi^2 = 76.8$ for 30 DOF; $\Delta\chi^2 = 33.1$) than for the fit in which the slope, a of the mass-concentration relation is also included as a free parameter (see above). We conclude that any analysis of redshift evolution in the mass-concentration relation should (at least) explore the full parameter space discussed above, with c_0 , a and b included as free parameters.

Finally, we have estimated the systematic scatter that may be present in the observed mass-concentration relation. This was carried out by modifying the χ^2 estimator to include an additional systematic uncertainty, and increasing the size of this systematic uncertainty until the reduced χ^2 value became equal to unity. Based on the fit with c_0 , a and b included as free parameters, we estimate an intrinsic systematic scatter in the data of $\Delta \log(c) \sim 0.1$, in good agreement with the predictions from simulations (e.g., Bullock et al. 2001; Wechsler et al. 2002).

In summary, the key results on the mass-concentration relation are 1) the presence of a tight, observed mass-concentration relation for massive, dynamically relaxed clusters. The measured normalization and estimated intrinsic, systematic scatter in this relation are consistent with the predictions from CDM simulations. 2) We observe a slope $a = -0.41 \pm 0.11$ (at 95 per cent confidence) for the mass-concentration relation that is significantly steeper than predicted by CDM simulations for lower mass halos ($a \sim -0.12$; Shaw et al. 2005). 3) The redshift evolution of the observed mass-concentration relation, $b = 0.54 \pm 0.47$ at 95 per cent confidence, is slower than, but marginally consistent with, the value of $b = 1$ in the Bullock et al. (2001) model.

3.3 The inner slope of dark matter profiles: generalized NFW models

For the final stage of our analysis, we have included the inner slope of the dark matter profile (α , in the generalized NFW model) as an additional free parameter in the fits with method 2. (Separate components to model the mass contributions from the X-ray emitting gas and the optically luminous matter in the central, dominant galaxies were included in the fits.)

The results on the inner mass profiles are summarized in Table 4. In terms of the goodness of fit, 27 out of 34 clusters give χ^2/DOF values with a probability of 0.05 or better. Of these 27 clusters, 21 have an inner slope consistent with unity at 68 per cent confidence.

In order to obtain a combined result on the inner dark matter profile, we have summed together the results on χ^2 as a function of α for the 27 clusters for which the generalized NFW model provides a reasonable description of the data. The results are shown in Fig. 3. (Note that we have subtracted the overall minimum summed χ^2 , of 75.37 for 72 DOF; 127 temperature measurements, 2 free parameters for 27 clusters and one free slope parameter).

From the summed χ^2 data we obtain a best-fitting inner slope of $\alpha = 0.88^{+0.26}_{-0.31}$, where the uncertainties are 95 per cent confidence limits. We conclude that our combined result

Table 5. Results on the virial masses M_{vir} (in units of $10^{14} h^{-1} M_{\odot}$) and concentration parameters $c_{\text{vir}} = r_{\text{vir}}/r_s$ of the dark matter halos for the standard NFW model (inner slope $\alpha = 1$ fixed). Uncertainties are 68 per cent confidence limits. If no error bar is quoted, the upper limit is unbounded and the lower limit is zero.

	c_{vir}	M_{vir}
Abell 1795	$5.79^{+1.08}_{-0.97}$	$6.30^{+2.10}_{-1.41}$
Abell 2029	$8.50^{+0.42}_{-0.47}$	$6.24^{+0.65}_{-0.49}$
Abell 478	$5.07^{+0.45}_{-0.41}$	$11.1^{+2.10}_{-1.79}$
PKS0745-191	$7.46^{+1.93}_{-1.33}$	$9.65^{+1.03}_{-3.00}$
Abell 1413	$5.62^{+0.96}_{-0.93}$	$7.71^{+2.39}_{-1.54}$
Abell 2204	$12.1^{+3.56}_{-2.64}$	$5.87^{+2.18}_{-1.47}$
Abell 383	$4.72^{+0.64}_{-0.83}$	$5.51^{+2.27}_{-1.16}$
Abell 963	$5.46^{+1.06}_{-1.07}$	$6.11^{+2.65}_{-1.53}$
RXJ0439.0+0521	$8.20^{+1.85}_{-1.46}$	$3.16^{+1.48}_{-0.97}$
RXJ1504.1-0248	$4.69^{+1.27}_{-1.32}$	$14.5^{+12.0}_{-4.82}$
RXJ2129.6+0005	$5.03^{+2.77}_{-2.38}$	$5.29^{+11.3}_{-2.65}$
Abell 1835	$4.23^{+0.54}_{-0.37}$	$17.6^{+4.00}_{-4.30}$
Abell 611	$6.17^{+2.04}_{-1.92}$	$5.44^{+4.00}_{-1.75}$
Zwicky 3146	$2.87^{+2.75}_{-2.75}$	$23.9^{+14.4}_{-14.4}$
Abell 2537	$5.86^{+2.75}_{-1.89}$	$6.07^{+5.03}_{-2.52}$
MS2137.3-2353	$8.65^{+0.68}_{-0.70}$	$3.67^{+0.65}_{-0.45}$
MACSJ0242.6-2132	$8.03^{+1.45}_{-1.08}$	$3.80^{+1.33}_{-1.05}$
MACSJ1427.6-2521	$8.56^{+2.69}_{-2.42}$	$2.31^{+1.94}_{-0.85}$
MACSJ2229.8-2756	$9.20^{+4.30}_{-3.08}$	$2.13^{+1.65}_{-0.80}$
MACSJ0947.2+7623	$6.47^{+2.18}_{-1.77}$	$8.44^{+6.96}_{-3.27}$
MACSJ1931.8-2635	$3.77^{+2.20}_{-2.23}$	$13.3^{+7.25}_{-7.25}$
MACSJ1115.8+0129	$2.22^{+2.56}_{-2.56}$	$34.2^{+26.0}_{-26.0}$
MACSJ1532.9+3021	$5.63^{+1.55}_{-1.46}$	$6.72^{+4.98}_{-2.23}$
MACSJ0011.7-1523	$3.75^{+0.99}_{-0.73}$	$8.39^{+4.51}_{-3.13}$
MACSJ1720.3+3536	$5.20^{+1.41}_{-1.03}$	$7.16^{+3.84}_{-2.69}$
MACSJ0429.6-0253	$9.00^{+1.82}_{-1.28}$	$2.82^{+0.88}_{-0.76}$
MACSJ0159.8-0849	$5.84^{+1.17}_{-1.24}$	$9.13^{+5.17}_{-2.67}$
MACSJ0329.7-0212	$5.57^{+0.87}_{-0.90}$	$5.20^{+2.10}_{-1.26}$
RXJ1347.5-1144	$5.63^{+0.78}_{-0.43}$	$25.1^{+4.90}_{-6.60}$
3C295	$9.07^{+1.19}_{-1.03}$	$2.74^{+0.64}_{-0.51}$
MACSJ1621.6+3810	$6.98^{+3.39}_{-2.24}$	$5.50^{+4.34}_{-2.30}$
MACSJ1311.0-0311	$5.17^{+1.59}_{-1.21}$	$4.88^{+3.04}_{-1.73}$
MACSJ1423.8+2404	$8.85^{+0.80}_{-0.90}$	$4.02^{+0.88}_{-0.59}$
MACSJ0744.9+3927	$4.92^{+1.60}_{-1.19}$	$6.81^{+3.89}_{-2.49}$

on the inner dark matter density slope is consistent with the range of values predicted by CDM simulations.

4 DISCUSSION

4.1 Previous results on the inner dark matter density slopes

Several of the clusters in the present sample have been the subjects of previous work that has examined the issue of the inner dark matter density slope. MS2137.3-2353 and Abell 963 were studied by Sand et al. (2002, 2004) using a combination of strong gravitational lensing data and optical velocity dispersion measurements for the dominant cluster galaxies. These authors measured surprisingly flat inner slopes for MS2137.3-2353, Abell 963 (which are formally consistent with the findings from the Chandra data presented in Table 4) and four other clusters, and concluded

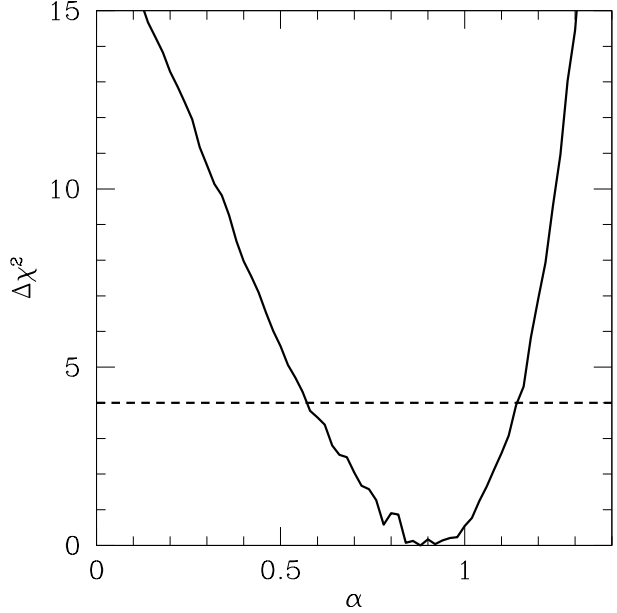


Figure 3. The summed χ^2 values as a function of the inner density slope α for the 27 clusters for which the generalized NFW model provides a reasonable fit to the data. The dotted lines indicate the 1, 2 and $3 - \sigma$ confidence limits. The overall best fit is obtained for $\alpha = 0.88^{+0.26}_{-0.31}$ (95 per cent confidence limits).

that their results were inconsistent with the standard NFW model ($\alpha = 1.0$) at 99 per cent confidence.

Later work by Bartelmann & Meneghetti (2004) and Dalal & Keeton (2003) cautioned that allowing for deviations from axial symmetry in the strong lensing analysis, using elliptical rather than spherical mass models (as motivated by the data) will modify the constraints on the inner dark matter profiles. These authors concluded that the strong lensing data of Sand et al. (2002, 2004) remain consistent with CDM models, once such effects are taken into account. The X-ray results presented here are also consistent with the standard NFW model ($\alpha = 1.0$) at 95 per cent confidence. It is important to note that X-ray data do not suffer in the same way from uncertainties regarding axial symmetry. For the regular, apparently relaxed clusters in the present sample, the mass models determined from the X-ray data under the assumption of spherical symmetry are unlikely to be affected by asphericity effects by more than a few per cent (Piffaretti et al. 2003; Gavazzi 2005).

Using Chandra data for Abell 2029 (the first ~ 20 ks observation only) and parameterized models for the gas density and temperature profiles, Lewis et al. (2003) obtained $\alpha = 1.19 \pm 0.04$ for the inner (total) mass profile. We measure $\alpha = 1.16^{+0.22}_{-0.34}$ for the dark matter at 68 per cent confidence using 94ks of clean data. (For the total mass, a fit with a generalized NFW model gives $\alpha = 1.16^{+0.26}_{-0.22}$). Thus, the present study and Lewis et al. (2003) obtain similar best-fit results, although the statistical uncertainties reported here are significantly larger, despite being based on more data. In part, this highlights the effects that priors, in the form of parameterized models for the gas density and temperature profiles, can have on the analysis. Zappacosta et al. (2006, see also

Buote & Lewis 2004) present a detailed study of the nearby, intermediate temperature cluster Abell 2589, for which they also model the dark matter, X-ray emitting gas and stellar mass associated with the cD galaxy separately. They conclude that the standard NFW model with $\alpha = 1$ provides a good description of the dark matter and total mass distributions in the cluster.

Arabadjis & Bautz (2004) studied Chandra data for Abell 1835, Abell 2029, Abell 2204, Zwicky 3146 and MS 2137.3-2353. Fig. 4 of that paper indicates best-fitting values of $\alpha \sim 1.85$ for Abell 2029, $\alpha \sim 1.8$ for Abell 2204, $\alpha \sim 0.9$ for Abell 1835, $\alpha \sim 1.7$ for Zwicky 3146 and $\alpha = 1.6 \pm 0.2$ for MS 2137.3-2353 (with 68 per cent confidence limits of $\sim 10-20$ per cent). In general, we find shallower inner dark matter slopes than Arabadjis & Bautz (2004). Our statistical uncertainties are also larger in some cases.

Voigt & Fabian (2006) present results on the inner slopes for 12 clusters, 8 of which are in common with the present study. These authors use a similar non-parametric spectral deprojection technique to measure the deprojected X-ray temperatures in the clusters. Their results on the central slope are in general agreement with those presented here.

4.2 On the robustness of the central galaxy model

Sand et al. (2002) present a detailed analysis of the optical properties of the dominant galaxy in MS2137.3-2353 (see also Gavazzi 2005). These authors fit a de Vaucouleurs profile to the galaxy surface brightness, yielding an effective radius $R_e = 5.02 \pm 0.50$ arcsec and a total V-band luminosity $L_V = 4.2 \times 10^{11} L_\odot$. Using the redshift-dependent V-band mass-to-light ratio of (Fukugita et al. 1998) and assuming a galaxy formation redshift ~ 2 , we obtain a V-band mass-to-light ratio for the dominant galaxy in MS2137.3-2353 of $M/L_V = 2.75$ and a total stellar mass of $1.14 \times 10^{12} M_\odot$. (The stellar mass dominates the total mass within 10 kpc of the center of the cluster. Note that Sand et al. (2002) measure an optical velocity dispersion for the dominant galaxy in MS2137.3-2353 of $\sigma \sim 275$ km/s, from which they infer $M/L_V \sim 3.1$; see also Gavazzi 2005 for a slightly lower M/L_V value). We have adopted these parameters as a template to approximate the mass contribution from stars in the central galaxies of all clusters in the sample, employing either a Jaffe model or de Vaucouleurs model.

In principle, we might expect the results on the inner dark matter density slopes to be sensitive to the choice of parameters used to describe the central stellar mass components. Here, the main systematic uncertainty lies with the assumption that the central stellar mass distribution in MS2137.3-2353 provides a reasonable model for other galaxy clusters in the sample. The assumption of a constant central stellar mass is well motivated; K-band observations of dominant cluster galaxies in X-ray luminous clusters (Brough et al. 2002) show little variation in total stellar mass over the redshift range $0 < z < 1$, with scatter at the level of 20–30 per cent.

To estimate of the effect of departures from a constant central stellar mass on the measured inner dark matter slopes, we have re-analysed the Chandra data for MS2137.3-2353 varying the M/L_V ratio over the range $M/L_V = 0-6$ (and thereby changing the central stellar mass by $\sim \pm 100$

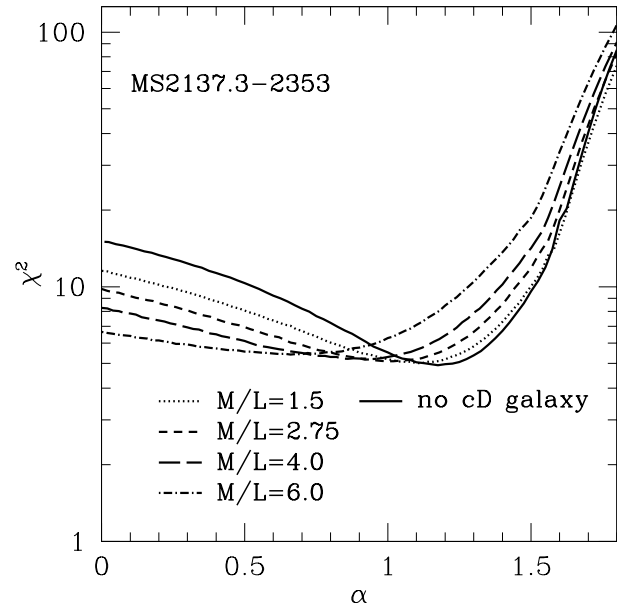


Figure 4. Goodness of fit for the inner slopes α for the galaxy cluster MS2137.3-2353. The mass model includes a Jaffe component for the luminous matter of the cD galaxy and a generalized NFW component for the dark matter halo.

per cent). In each case, we have re-determined the constraints on the inner slope α . The results are shown in Fig. 4. Note that MS2137.3-2353 is one of the least massive clusters in the sample, and so changes in α with central stellar mass are likely to be larger than for most other clusters in the sample. For $M/L_V = 1.5$, we measure $\alpha = 1.10_{-0.30}^{+0.22}$ at 68 per cent confidence. For $M/L_V = 4$, we measure $\alpha = 0.94_{-0.46}^{+0.24}$. The tendency is for higher M/L_V ratios to give slightly shallower inner dark matter slopes. These results can be compared to the best-fitting result for MS2137.3-2353 with $M/L_V = 2.75$ of $\alpha = 1.00_{-0.35}^{+0.25}$. We conclude that the results on the inner dark matter slope for MS2137.3-2353 are robust against changes in the central stellar mass by ± 50 per cent.

Finally, we note that extending the analysis to model the mass components associated with stars external to central galaxies separately should have a negligible effect on the results. In total, stars contribute only ~ 2 per cent of the total cluster mass (e.g., Lin & Mohr 2004; Fukugita et al. 1998).

In conclusion, the results presented here are robust against systematic uncertainties associated with measuring the stellar mass contribution in the clusters.

4.3 Residual systematic uncertainties

The clusters studied here are the most massive, dynamically relaxed clusters known and are, therefore, the systems for which the assumption of hydrostatic equilibrium should be most robust. Although, as discussed above, geometric effects and uncertainties associated with separating the dark matter and baryonic matter components are unlikely to impact

on the results significantly, some systematic uncertainties remain.

In the first case, it remains possible that small levels of non-thermal pressure support due to *e.g.* gas motions, cosmic rays or magnetic fields could be present in the X-ray emitting gas and bias the measured masses low. However, the relaxed nature of the clusters argues that large, unaccounted for, bulk and/or turbulent motions are unlikely to be present and that the mass measurements should be recovered to better than 10-20 per cent accuracy (Nagai *et al.* 2006; Rasia *et al.* 2006). Galaxy clusters are known to contain magnetic fields (*e.g.*, Carilli & Taylor 2002) The issue of magnetic pressure support and its effect on X-ray mass measurements has been studied by Dolag & Schindler (2000) who showed that for relaxed clusters, magnetic pressure support is unlikely to bias mass measurements significantly, even in the central regions. For individual clusters, effects no larger than 10-20 per cent are expected. The similarity of the mass results obtained using method 1, where we measure the total mass and method 2, where we model the dark and baryonic components separately, also argues that any non-thermal pressure component, at the $\sim 10 - 15$ per cent level, distributed in a similar manner to the dark or baryonic matter, is unlikely to have a significant effect on the conclusions. A program to determine the maximum size of non-thermal pressure in the clusters, using a combination of Chandra X-ray data and wide field weak gravitational lensing observations, is underway (Donovan *et al.*, in preparation).

It should also be recognized that although we quote results on the mass-concentration relation appropriate for the virial radii in the clusters, thereby allowing an easy comparison with the predictions from simulations, the X-ray data only extend to about r_{2500} or approximately a quarter to a third of the virial radius in most clusters. Some systematic uncertainty is associated with extrapolating the allowed range of NFW mass models to these larger radii.

Finally, we reiterate that the simulations used to predict the mass-concentration relation and central dark matter slopes (*e.g.*, Navarro *et al.* 1995, 1997; Diemand *et al.* 2004; Shaw *et al.* 2005) are CDM only. In detail, these predictions may be modified by future numerical work that includes the X-ray emitting gas and stars, and realistic baryonic physics (cooling, star formation, AGN feedback). For the most accurate comparison with the data presented here, such simulations should contain a sufficiently large number of massive, relaxed clusters and be normalized to match the observed X-ray (*e.g.*, temperature profiles, virial relations, X-ray gas mass fraction; Allen *et al.* 2001, 2004; Vikhlinin *et al.* 2006) and optical (Croton *et al.* 2006; Bower *et al.* 2006) properties.

5 SUMMARY

We have used the Chandra X-ray Observatory to measure the dark matter and total mass profiles for a sample of 34 massive, dynamically relaxed galaxy clusters. Our analysis has employed a non-parametric, spherical deprojection technique that minimizes the need for priors associated with parameterized models for the X-ray gas density and/or temperature profiles. This allows a direct assessment of the good-

ness of fit to the Chandra data provided by a variety of simple mass models as well as an accurate determination of statistical uncertainties on fit parameters.

We have shown that the NFW model, which is motivated by CDM simulations, provides a good description of the total mass and dark matter distributions in the majority of clusters. In contrast, the singular isothermal sphere model can, in almost every case, be firmly ruled out. Combining the results for all clusters for which the NFW model provides an acceptable description of the dark matter profiles, we obtain a best-fitting result on the inner slope of the dark matter density profile in the clusters, $\alpha = 0.88^{+0.15}_{-0.11}$ (68 per cent confidence limits).

We observe a well-defined mass-concentration relation for the clusters with a normalization and intrinsic scatter in good agreement with the predictions from simulations. The slope of the mass-concentration relation, $c \propto M_{\text{vir}}^a / (1+z)^b$ with $a = -0.41 \pm 0.11$ at 95 per cent confidence, is significantly steeper than the value of $a \sim -0.1$ predicted by CDM simulations for lower mass halos. The redshift evolution, $b = 0.54 \pm 0.47$ at 95 per cent confidence, is also slower than, but marginally consistent with, the value $b \sim 1$ predicted by those simulations.

ACKNOWLEDGMENTS

We thank Laurie Shaw for kindly providing the simulated data from Shaw *et al.* (2005) and Adam Mantz and Glenn Morris for helpful discussions. We thank our collaborators in the ongoing cluster cosmology work, especially H. Ebeling for his heroic efforts in compiling the MACS sample. We are grateful to the developers of the GNU Octave numerical computation language and the GNU Scientific Library for their ongoing efforts. This work was supported in part by the U.S. Department of Energy under contract number DE-AC02-76SF00515 and by the National Aeronautics and Space Administration through Chandra Award Number DD5-6031X issued by the Chandra X-ray Observatory Center, which is operated by the Smithsonian Astrophysical Observatory for and on behalf of the National Aeronautics and Space Administration under contract NAS8-03060.

REFERENCES

- Abramowitz M., Stegun I.A., 1965, Dover, New York
- Allen S.W., Ettori S., Fabian A.C., 2001, MNRAS, 324, 877
- Allen S.W., Schmidt R.W., Fabian A.C., 2001, MNRAS, 328, 37
- Allen S.W., Schmidt R.W., Fabian A.C., 2002, MNRAS, 335, 256
- Allen S.W., Schmidt R.W., Ebeling H., Fabian A.C., van Speybroeck L., 2004, MNRAS, 353, 457
- Allen S.W., Fabian A.C., Johnstone R.M., Edge A.C., Nulsen P.E.J., 1992, MNRAS, 254, 51
- Andersson K.E., Madejski G.M., 2004, ApJ, 607, 190
- Arnaud K.A., 1996, Astronomical Data Analysis Software and Systems V, eds. Jacoby G. and Barnes J., p17, ASP Conf. Series volume 101

- Arabadjis J.S., Bautz M.W., 2004, submitted to ApJ, preprint astro-ph/0408362
- Arabadjis J.S., Bautz M.W., Garmire G.P., 2002, ApJ, 572, 66
- Ascasibar Y., Markevitch M., 2006, ApJ, submitted, preprint astro-ph/0603246
- Balucinska-Church M., McCammon D., 1992, ApJ, 400, 699
- Bartelmann M., Meneghetti M., 2004, A&A, 418, 413
- Birzan L., Rafferty D.A., McNamara B.R., Wise M.W., Nulsen P.E.J., 2004, ApJ, 607, 800
- Böhringer H., Voges W., Fabian A.C., Edge A.C., Neuman D.M., 1993, MNRAS, 264, 25
- Bower R.G., Benson A.J., Malbon R., Helly R., Frenk C.S., Baugh C.M., Cole S., Lacey C.G., 2005, MNRAS, submitted, preprint astro-ph/0511338
- Brough S., Collins C.A., Burke D.J., Mann R.G., Lynam P.D., 2002, MNRAS, 329, L53
- Bullock J.S., Kolatt T.S., Sigad Y., Somerville R.S., Kravtsov A.V., Klypin A.A., Primack J.R., Dekel A., 2001, MNRAS, 321, 559
- Buote D.A., Canizares C.R., 1996, ApJ, 457, 565
- Buote D.A., Lewis A.D., 2004, ApJ, 604, 116
- Carilli C.L., Taylor G.B., 2002, ARA&A, 40, 319
- Cavaliere A., Fusco-Femiano R., 1978, A&A, 70, 677
- Croton D.J. et al. 2006, MNRAS, 365, 11
- Dalal N., Keeton C.R., 2003, preprint astro-ph/0312072
- de Vaucouleurs G., 1948, Ann. d'Ap, 11, 247
- Diemand J., Moore B., Stadel J., 2004, MNRAS, 353, 624
- Diemand J., Zemp M., Moore B., Stadel J., Carollo M., 2005, MNRAS, 364, 665
- Dolag K., Schindler S., 2000, A&A, 364, 491
- Dolag K., Bartelmann M., Perrotta F., Baccigalupi C., Moscardini L., Meneghetti M., Tormen G., 2004, A&A, 416, 853
- Dunn R.J.H., Fabian A.C., 2004, MNRAS, 355, 862
- Dunn R.J.H., Fabian A.C., Taylor G.B., 2005, MNRAS, 364 1343
- Fabian A.C., Sanders J.S., Ettori S., Taylor G.B., Allen S.W., Crawford C.S., Iwasawa K., Johnstone R.M., Ogle P.M., 2000, MNRAS, 318, L65
- Fabian A.C., Sanders J.S., Allen S.W., Crawford C.S., Iwasawa K., Johnstone R.M., Schmidt R.W., Taylor G.B., 2003, MNRAS, 344, L43
- Fabian A.C., Sanders J.S., Taylor G.B., Allen S.W., Crawford C.S., Johnstone R.M., Iwasawa K., 2006, MNRAS, 366, 417
- Forman W. et al., 2005, ApJ, 635, 894
- Fukugita M., Hogan C.J., Peebles P.J.E., 1998, ApJ 503, 518
- Gavazzi R., 2005, A&A, 443, 793
- Gavazzi R., Fort B., Mellier Y., Pelló R., Dantel-Fort M., 2003, A&A, 403, 11
- Hernquist L., 1990, ApJ, 356, 359
- Jaffe W., 1983, MNRAS, 202, 995
- Jing Y.P., & Suto Y., 2000, ApJL, 529, L69
- Kaastra J.S., Mewe R., 1993, Legacy, 3, 16
- Klypin A., Kravtsov A.V., Bullock J.S., Primack J.R., 2001, ApJ, 554, 903
- Kuhlen M., Strigari L.E., Zentner A.R., Bullock J.S., Primack J.R., 2005, MNRAS, 357, 387
- Lewis A.D., Stocke J.T., Buote D.A., 2002, ApJL, 573, L13
- Lewis A.D., Buote D.A., Stocke J.T., 2003, ApJ, 586, 135
- Liedahl D.A., Osterheld A.L., Goldstein W.H., 1995, ApJ, 438, L115
- Lin Y.-T., Mohr J.J., 2004, ApJ, 617, 879
- Marquardt D.W., 1963, Journal of the Society for Industrial and Applied Mathematics, 11, 431
- Meneghetti M., Bartelmann M., Jenkins A., Frenk C., 2005, preprint astro-ph/0509323
- Markevitch M., Vikhlinin A., Mazzotta P., 2001, ApJ, 562, L153
- Moore B., Quinn T., Governato F., Stadel J., Lake G., 1999, MNRAS, 310, 1147
- Nagai D., Vikhlinin A., Kravtsov A.V., 2006, ApJ, submitted, preprint astro-ph/0609247
- Navarro J.F., Frenk C.S., White S.D.M., 1995, MNRAS, 275, 720
- Navarro J.F., Frenk C.S., White S.D.M., 1996, ApJ, 462, 563
- Navarro J.F., Frenk C.S., White S.D.M., 1997, ApJ, 490, 493
- Navarro J.F. et al., 2004, MNRAS, 349, 1039
- Piffaretti R., Jetzer P., Schindler S., 2003, A&A, 398, 41
- Pointecouteau E., Arnaud M., Pratt G.W., 2005, A&A, 435, 1
- Rafferty D.A., McNamara B.R., Nulsen P.E.J., Wise M.W., 2006, ApJ, in press, preprint astro-ph/0605323
- Rasia E. et al. 2006, MNRAS, 369, 2013
- Sand D.J., Treu T., Ellis R.S., 2002, ApJL, 574, L129
- Sand D.J., Treu T., Smith G.P., Ellis R.S., 2004, ApJ, 604, 88
- Sand D.J., Treu T., Ellis R.S., Smith G.P., 2005, ApJ, 627, 32
- Schmidt R.W., Allen S.W., Fabian A.C., 2001, MNRAS, 327, 1057
- Shaw L., Weller J., Ostriker J.P., Bode P., 2005, preprint astro-ph/0509856
- Smith G.P., Kneib J.-P., Ebeling H., Czoske O., Smail I., 2001, ApJ, 552, 493
- Tsatsisomi A., Kravtsov A.V., Wechsler R.H., Primack J.R., 2004, ApJ, 614, 533
- Vikhlinin A., Kravtsov A., Forman W., Jones C., Markevitch M., Murray S.S., Van Speybroeck L., 2006, ApJ, 640, 691
- Voigt L.M., Fabian A.C., 2006, MNRAS, 368, 518
- Wechsler R.H., Bullock J.S., Primack J.R., Kravtsov A.V., Dekel A., 2002, ApJ, 568, 52
- Weisskopf M.C., Tananbaum H.D., Van Speybroeck L.P., O'Dell S.L., 2000, SPIE 4012, 2
- White, D.A., Jones C., Forman W., 1997, MNRAS, 292, 419
- Wiythe J.S.B., Turner E.L., Spergel D.N., 2001, ApJ, 555, 504
- Young P.J., 1976, AJ 81, 807
- Zappacosta L., Buote D.A., Gastaldello F., Humphrey P.J., Bullock J., Brighenti F., Mathews W., 2006, preprint astro-ph/0602613
- Zhang Y.Y., Böhringer H., Finoguenov A., Ikebe Y., Matsushita K., Schuecker P., Guzzo L., Collins C.A., 2006, A&A, in press, preprint astro-ph/0603275
- Zhao H., 1996, MNRAS, 278, 488
- Zhao D.H., Jing Y.P., Mo H.J., Börner G., 2003, ApJL, 597, L9

This paper has been typeset from a \TeX / \LaTeX file prepared
by the author.